Supporting Information

Gebbie et al. 10.1073/pnas.1508366112

Dynamic Forces

When bringing the mica surfaces together, we found dynamic forces to be unmeasurably small, within error, for the approach rates we report in this manuscript (5–10 Å/s). In contrast, we always measure dynamic attractive forces when separating the two surfaces, even for separation rates as slow as 2 Å/s (Fig. S1). These attractive dynamic forces are much stronger than those that would be predicted via traditional hydrodynamic drag models that assume continuum fluids of bulk viscosity.

From a molecular point of view, the magnitudes of these dynamic forces should be significantly larger on separation than on approach, in agreement with our experimental results, due to differences in the fluid flow mechanisms when the RTIL ions flow out of, rather than into, nanoconfined gaps. The expulsion of ions out of confined spaces should only involve molecular motions on the order of a single ion-pair diameter for single-layer instabilities.

In contrast, the fluid must be moved out of the bulk reservoir and into the entire micrometer-scale area of the nanoconfined interface as two surfaces are pulled apart, involving the motion of many RTIL ions over distances that are extremely large compared with the size of the individual ions. This is likely a much slower and more complex process than the expulsion of ions. Separation rates on the order of angstroms per minute or even angstroms per hour would likely be required to avoid overloading the spring and inducing additional nonequilibrium dynamic attractions as the surfaces are separated. Unfortunately, such slow separation rates are impractical for our experiments, as we need to collect dozens of force runs at different temperatures.

Short-Range Nonmonotonic Forces and Colloidal Stability

The nonmonotonic features (~0.5-nm plateaus) in the force–distance profiles correspond to "oscillatory" transitions, where ordered layers of ions are forced out from between the mica surfaces and into the bulk reservoir (Figs. S2 and S3). Given the highly correlated nature of strongly interacting RTIL ions, we expect that these ion layers consist of both cations and anions but are enriched in cations, due to the negative mica surface potential. The surface separation distance at which we detect the first oscillation is $D \approx 5$ nm (~2.5 nm per surface) for both $[C_2mim][NTf_2]$ and $[C_3mim][NTf_2]$, in agreement with previous measurements across other RTILs (21–25). Assuming that the plateau distance of ~0.5 nm for each RTIL corresponds to a characteristic effective molecular "diameter" for each ion pair, this would mean that the RTILs form solvation layers of about five molecular "diameters" in thickness per surface.

As the temperature is raised, the number and location of observed ion layers remains unchanged, and the layers are forced out of the interface under similar compressions, with an observed likelihood of being removed under slightly decreased pressures at increased temperatures. This observation suggests that the ions pack into similar surface-induced structures for the entire temperature range of 22–75 °C. Perhaps the strong coulombic interactions between RTIL ions enables them to maintain surface-induced structures at these elevated temperatures. However, the solvation layers formed by cyclohexane confined between mica surfaces was also observed to remain unchanged between 22–41 °C (40).

At all temperatures, the surfaces begin to progressively flatten under very large applied loads ($F > 10$ mN). Once the surfaces enter this regime of flattening, the surface area increases in proportion to the load, so the pressure applied to the strongly bound ion layers stays approximately constant. As a result, no additional ions are forced out of the interface. For $[C_2mim][NTf_2]$, the final film thickness was measured to be ~2.5 nm under high loads. Thus, we conclude that the measured final film thickness of ~2.5 nm corresponds to a confined structure consisting of between four and six total layers of ions between the surfaces (two or three ion layers per surface). The final film thickness increases to ~3 nm for $[C_3mim][NTf_2]$. Since the $[C_3mim]^+$ cation is larger than the $[C_2mim]^+$ cation by only one $–CH_2–$ group, the final number of confined ion layers most likely corresponds to the same number of ion layers or, at most, one additional ion layer at high compressions (two to four per surface) for $[C_3mim][NTf_2]$.

In comparison, seminal experiments on the formation of (room-temperature) solvation layers by traditional liquids demonstrate that the range of surface-induced layering can be as short as 1 nm per (mica) surface for small, highly mobile molecules such as water (41), and as long as 4.5 nm per (mica) surface for octamethylcyclotetrasiloxane (42), a large oblate spheroid molecule. For a wide variety of polar and nonpolar liquids confined between mica surfaces, liquids typically form solvation layers that extend to distances of about five molecular diameters (of the liquid) per surface at room temperature (40–42). These layers result in alternating repulsive and attractive "oscillatory" contributions to the force–distance profiles measured across confined liquids, analogous to those measured across RTILs. For traditional liquids, these "oscillatory" forces are always superimposed with the van der Waals and electric double-layer forces of standard Derjaguin–Landau–Verwey–Overbeek theory (40–42).

For $[C_2mim][NTf_2]$ and $[C_3mim][NTf_2]$ confined between mica surfaces, these "oscillatory" solvation forces are clearly superimposed with a strongly repulsive electrostatic force, as shown in Fig. 3 of the main text. Surface–surface van der Waals interactions also occur across RTILs, and the dielectric/optical properties of RTILs should be used to account for the screening of van der Waals attractions. In the current study, the combination of strongly repulsive double-layer and solvation forces overwhelms the van der Waals attraction down to the final measured separation distances of $D \sim 2.5$–3 nm.

Although the formation of solvation layers by RTILs in contact with solid surfaces is one of the most widely discussed aspects of RTIL interfacial behavior, we conclude that RTILs show a propensity for forming solvation layers that is very similar to that exhibited by many other polar and nonpolar liquids.

The practical implication of this conclusion is that the solvation layers formed by RTILs should be viewed as fundamentally similar to the solvation layers formed by other liquids. Namely, these solvation layers will indeed contribute to colloidal stability, but the ultimate dispersion (aggregation) state of colloidal particles immersed in RTILs will also critically depend on van der Waals and electrostatic interactions. After all, a knowledge of solvation interactions alone is not sufficient to predict the colloidal stability of particles immersed in other liquids that form solvation structures of comparable ranges and magnitudes.

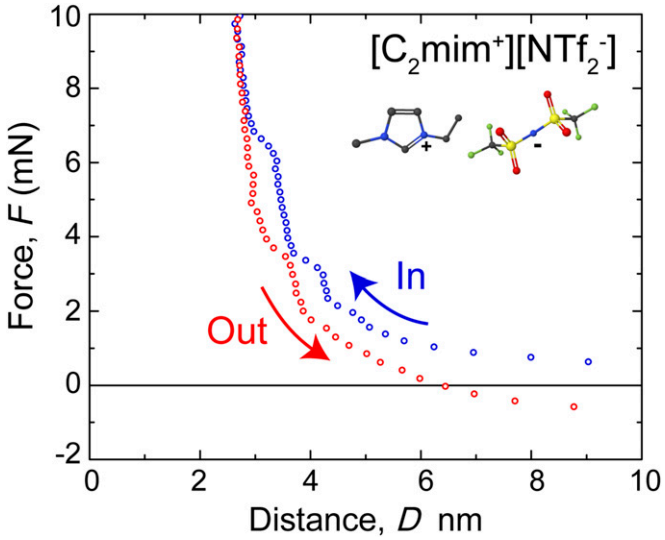


Fig. S1. Representative short-range interaction forces measured across $[C_2mim][NTf_2]$ at 22 °C with $R = 1$ cm surfaces on approach (blue) and separation (red). The y axis is presented in units of force, F (without R normalization), because the Derjaguin approximation fails within the "oscillatory" regime due to a combination of surface deformation and curvature effects. On separation, we still observe evidence of solvation and double-layer forces; however, these equilibrium forces are superimposed on an additional weakly attractive dynamic force. This dynamic attractive force results from separating of the surfaces at rates that exceed the extremely long times required for the viscous RTILs to flow back into the interface under equilibrium conditions. Thus, the red points should not be interpreted as true equilibrium forces. In the absence of dynamic effects and/or energy dissipation, the forces measured when separating the two surfaces should exactly overlay the forces measured when bringing the two surfaces together.

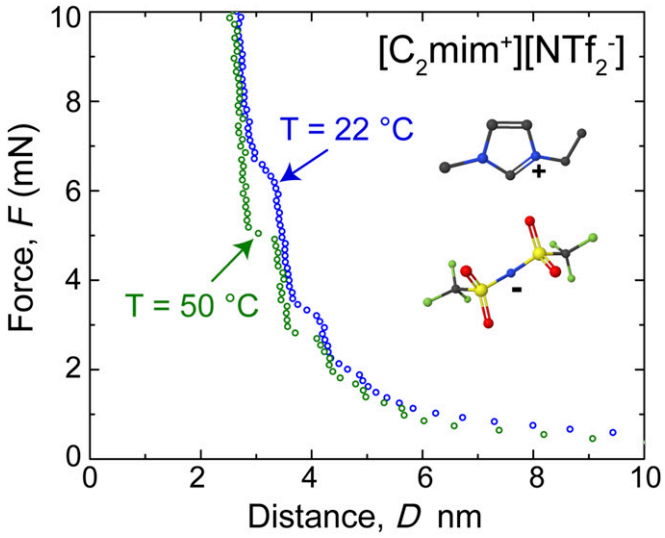


Fig. S2. Representative short-range interaction forces measured across $[C_2mim][NTf_2]$ with $R = 1$ cm surfaces at room temperature (blue) and 50 °C (green). The y axis is presented in units of force, F (without R normalization), because the Derjaguin approximation fails within the "oscillatory" regime due to a combination of surface deformation and curvature effects. For the room-temperature force profile (blue), $(\kappa^*)^{-1} = 6.7$ nm and $\psi = 80$ mV. For the 50 °C force profile (green), $(\kappa^*)^{-1} = 4.2$ nm and $\psi = 100$ mV.

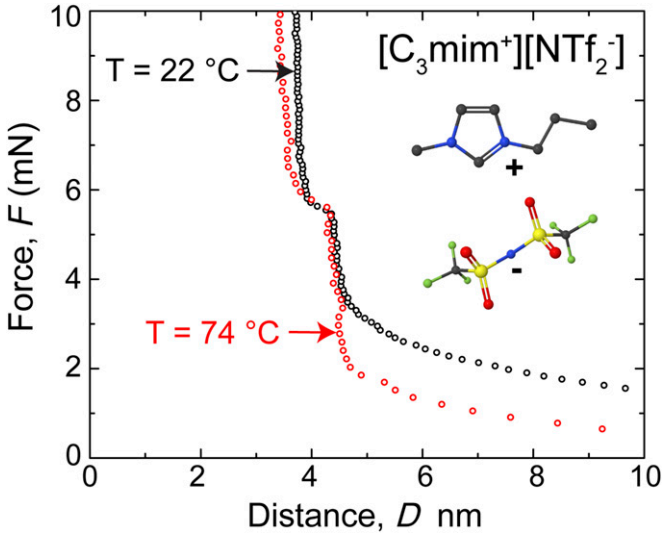


Fig. S3. Representative short-range interaction forces measured across $[C_3mim][NTf_2]$ with $R = 5$ cm surfaces at room temperature (black) and 74 °C (red). The y axis is presented in units of force, F (without R normalization), because the Derjaguin approximation fails within the "oscillatory" regime due to a combination of surface deformation and curvature effects. For the room-temperature force profile (black), $(\kappa^*)^{-1} = 7.5$ nm and $\psi = 67$ mV. For the 74 °C force profile (red), $(\kappa^*)^{-1} = 3.3$ nm and $\psi = 40$ mV.

Table S1. $[C_2mim][NTf_2]$ interaction parameters fitted with Eq. 1

Temperature, °C	Experiment	Run	Effective Debye length $(\kappa^*)^{-1}$, nm	Mica potential ψ, mV
22	1	1	6.83	99
22	1	2	6.60	84
22	1	3	6.87	97
22	1	4	6.56	96
22	1	5	6.70	72
22	1	6	6.52	100
22	1	7	6.57	102
22	1	8	6.88	80
22	1	9	6.71	80
22	1	10	6.81	70
22	2	1	6.85	102
22	2	2	6.59	104
22	2	3	6.76	117
22	2	4	6.86	129
22	2	5	6.77	94
22	2	6	6.45	85
22	3	1	6.81	134
22	3	2	6.75	142
22	3	3	6.66	143
22	3	4	6.60	114
22	4	1	6.71	82
22	4	2	6.83	71
22	4	3	7.08	74
22	4	4	6.95	69
22	4	5	6.81	80
22	4	6	6.42	81
22	4	7	6.73	100
22	4	8	6.50	103
22	5	1	6.62	65
22	5	2	6.56	56
22	5	4	6.92	59
22	5	5	6.89	57
22	5	6	6.98	64
40	1	11	5.75	94
40	1	12	5.60	77
40	1	13	5.45	77
40	1	14	5.71	85
40	1	15	5.87	103
40	1	16	5.74	102
40	1	17	5.83	97
40	1	18	5.73	88
40	1	19	5.62	89
40	1	20	5.87	101
40	1	21	5.84	95
40	1	22	5.95	103
40	1	23	5.53	91
40	3	5	5.67	90
40	3	6	5.37	107
40	3	7	5.58	123
40	3	8	5.46	137
40	3	9	5.81	79
40	3	10	5.73	151
40	3	11	5.74	110
40	3	12	5.59	102
50	3	13	4.16	106
50	3	14	4.03	82
50	3	15	4.57	93
50	3	16	4.76	110
50	3	17	4.62	110
50	3	18	4.56	158
50	3	19	3.55	123
50	3	20	4.60	111

Table S1. Cont.

Temperature, °C	Experiment	Run	Effective Debye length $(\kappa^*)^{-1}$, nm	Mica potential ψ, mV
50	5	7	4.62	63
50	5	8	4.73	55
50	5	9	4.56	62
50	5	10	4.43	71
50	5	11	3.51	50
50	5	12	3.60	56
50	5	13	4.67	68
60	1	24	3.63	117
60	1	25	2.97	72
60	1	26	3.56	131
60	1	27	3.55	120
60	1	28	3.54	127
60	1	29	3.71	81
60	1	30	3.53	113
60	1	31	3.75	115
60	1	32	3.32	65
60	1	33	3.83	128
60	1	34	3.39	75
60	4	9	3.43	125
60	4	10	3.36	95
60	4	11	3.03	101
60	4	12	3.23	104
60	4	13	3.60	117
60	4	14	3.70	100
60	4	15	3.61	120
60	4	16	3.05	142
60	4	17	3.23	122
60	4	18	3.29	91
60	4	19	3.38	100
60	4	20	3.38	122
60	4	21	3.37	166

Table S2. $[C_3mim][NTf_2]$ interaction parameters fitted with Eq. 1

Temperature, °C	Experiment	Run	Effective Debye length $(\kappa^*)^{-1}$, nm	Mica potential ψ, mV
22	1	1	7.44	62
22	1	2	7.43	69
22	1	3	7.48	69
22	1	4	7.46	65
22	1	5	7.45	66
22	1	6	7.52	71
22	1	7	7.42	50
22	2	1	7.51	72
22	2	2	7.57	73
22	2	3	7.40	74
22	2	4	7.59	75
22	2	5	7.42	68
22	2	6	7.44	71
22	2	7	7.53	70
22	2	8	7.46	70
22	2	9	7.58	75
22	2	10	7.41	74
22	2	11	7.58	80
22	2	12	7.47	79
22	3	1	7.39	82
22	3	2	7.30	87
22	3	3	7.45	80
22	3	4	7.47	76
22	4	1	7.35	82
22	4	2	7.33	82
22	4	3	7.24	75
30	2	8	6.65	75
30	2	9	6.88	81
30	2	10	6.60	81
30	2	11	6.69	83
30	2	12	6.81	85
30	2	13	6.54	75
30	2	14	6.87	77
33	1	8	6.30	59
33	1	9	6.66	63
33	1	10	6.45	66
33	1	11	6.33	71
33	1	12	6.37	72
33	1	13	6.58	74
33	1	14	6.37	73
33	1	15	6.58	74
33	1	16	6.37	75
33	1	17	6.58	74
33	1	18	6.37	73
33	1	19	6.58	74
33	1	20	6.37	75
33	1	21	6.54	79
33	1	22	6.45	78
33	1	23	6.81	83
33	1	24	6.82	85
45	1	25	5.41	69
45	1	26	5.25	66
45	1	27	5.87	61
45	1	28	5.94	63
45	1	29	5.84	73
45	1	30	6.20	70
45	1	31	5.57	70
45	1	32	5.45	64
45	1	33	6.03	68
45	2	15	5.17	66
45	2	16	5.44	68
45	2	17	5.58	67

Table S2. Cont.

Temperature, °C	Experiment	Run	Effective Debye length $(\kappa^*)^{-1}$, nm	Mica potential ψ, mV
45	2	18	5.06	57
45	2	19	4.20	61
45	2	20	5.96	70
74	1	40	3.75	51
74	1	41	3.22	37
74	1	42	3.38	44
74	1	43	3.75	45
74	1	44	3.57	38
74	1	45	3.44	57
74	1	46	3.30	45
74	1	47	3.49	58
74	1	48	3.72	67
74	1	49	3.56	65
74	1	50	3.77	68
74	1	51	3.23	50